Dense and Sparse Labeling with Multi-Dimensional Features for Saliency Detection

Yuchen Yuan, *Student Member, IEEE*, Changyang Li, *Member, IEEE*, Jinman Kim, *Member, IEEE*, Weidong Cai, *Member, IEEE*, and David Dagan Feng, *Fellow, IEEE*

***Abstract*—Conventional low-level feature based saliency detection methods tend to use non-robust prior knowledge and do not perform well in complex or low-contrast images. In this paper, to address the issues above in existing methods, we propose a novel deep neural network (DNN) based dense and sparse labeling (DSL) framework for saliency detection. DSL consists of three major steps, namely dense labeling (DL), sparse labeling (SL) and deep convolutional (DC) network. The DL and SL steps conduct initial saliency estimations with macro object contours and low-level image features, respectively, which effectively approximate the location of the salient object and generate accurate guidance channels for the DC step; the DC step, on the other hand, takes in the results of DL and SL, establishes a 6-channeled input data structure (including local superpixel information), and conducts accurate final saliency classification. Our DSL framework exploits the saliency estimation guidance from both macro object contours and local low-level features, as well as utilizing the DNN for high-level saliency feature extraction. Extensive experiments are conducted on six well-recognized public datasets against sixteen state-of-the-art saliency detection methods, including ten conventional feature based methods and six learning based methods. The results demonstrate the superior performance of DSL on various challenging cases in terms of both accuracy and robustness.**

***Index Terms*—Saliency detection, deep neural network, dense labeling, sparse labeling, macro object contour, low-level feature**

I. Introduction

SALIENCY detection, which originates from the contrast detection of human visual system [3], has experienced drastic developments in the researches of computer vision in recent years. Its ultimate goal is to mimic the intrinsic functions of human visual system, by which the understanding of the surrounding environment can be conducted accurately and effortlessly. Since emergence, saliency detection is functioning as an important preprocessing step in computer vision, which is widely applied in various image analysis tasks such as image segmentation [4], object detection [5], [6], object tracking [7], picture collaging [8], [9], and color filtering [10], [11], etc.

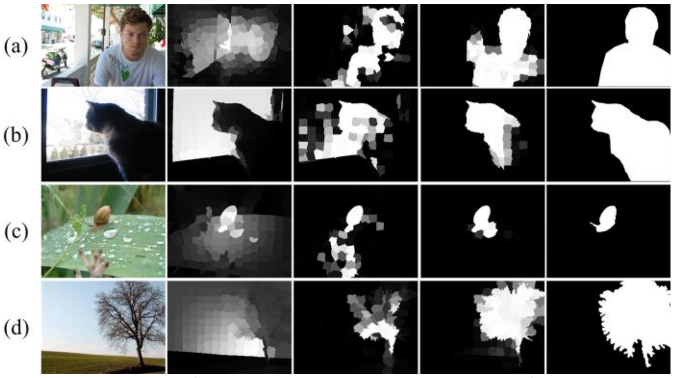

Fig. 1. A glimpse of our proposed DSL method. From left to right: input images; saliency maps by a low-level feature based method [1]; saliency maps by a learning based method [2]; saliency maps by DSL; ground truth.

Early researches of saliency detection mostly focus on human eye fixation [3], [12], [13], which approximates the visual attention of semantic objects in a given image, such as human faces, texts, or daily objects [12], [14]. The detection results of eye fixations, however, are often presented as sparse dots without details about the objects. On the other hand, the recently emerged salient object detection is capable of locating and segmenting the whole salient object with complete boundary details [15], and hence has received broad research interests.

Salient object detection (or simply saliency detection) aims to locate the most informative and attention-catching object in an image [16]. To achieve such objective, an intuitive way is to take advantage of the low-level features within the input image itself, which is the core idea of most conventional saliency detection methods. These features include but are not limited to: color [3], [13], histogram [17], [18], spatial distribution [19], [20], color filter response [10], [11], spectrum [21], [22], data architecture [1], [23], and background prior [24], [25], etc. These low-level feature based saliency detection methods are usually efficient to conduct, since no training process is involved. They have shown promising results both in bottom-up approaches [21], [26-30] and in top-down approaches [18], [31], [32]. Nevertheless, at least three major drawbacks hinder their performances: (1) Without feature abstraction and learning, their hand-crafted low-level features are only effective on relatively high contrast images and do not perform well on images with complex foreground / background contexts. This drawback, however, can be readily solved via high-level feature learning, which is seen in Fig. 1a. (2) Most of the prior knowledge applied in low-level feature based methods

Y. Yuan, C. Li, J. Kim, and W. Cai are with the Biomedical & Multimedia Information Technology (BMIT) Research Group, School of Information Technologies, The University of Sydney, Darlington, NSW 2008, Australia. E-mail: {yuchen.yuan, changyang.li, jinman.kim, tom.cai}@sydney.edu.au.
D. D. Feng is with the BMIT Research Group, and also with the Med-X Research Institute, Shanghai Jiaotong University, Shanghai 200030, China. E-mail: dagan.feng@sydney.edu.au.

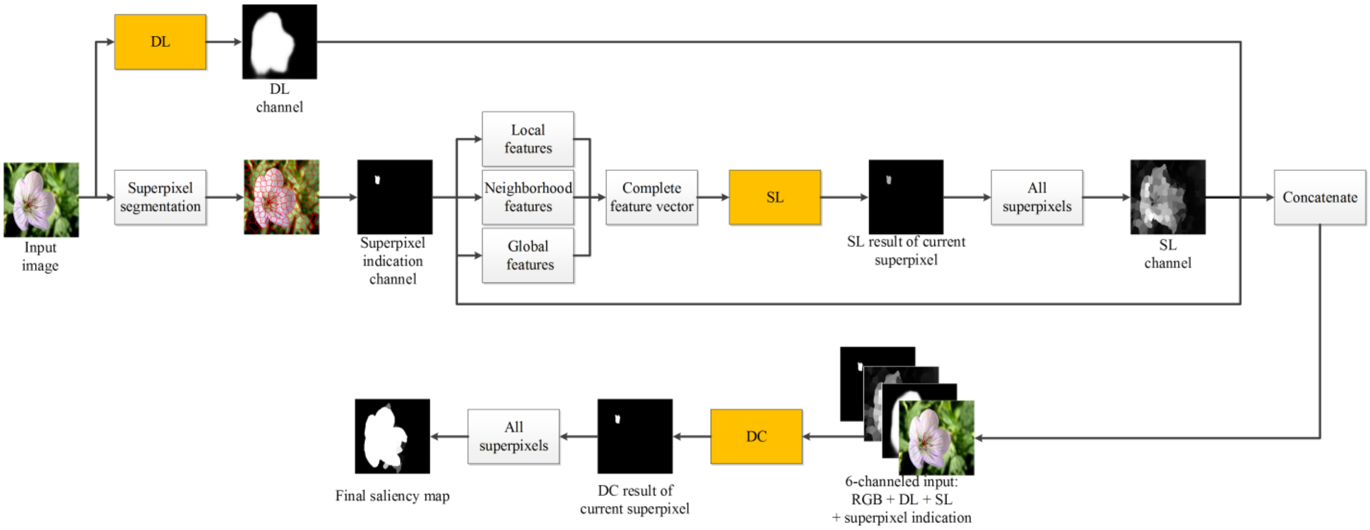

Fig. 2. Flowchart of our DSL method. The three major steps DL, SL and DC are highlighted in yellow. An input image is first processed by DL and SL, respectively; the resulting initial saliency estimations are then concatenated with the image RGB channels and the superpixel indication channel to form the 6-channel input of DC, which is used to generate the final saliency map.

is largely empirical with specific pre-assumptions, e.g. image boundary regions are assumed as background [1], [25], or image center regions are assumed as foreground [19], [33]. These pre-assumptions are easily violated on broader datasets with more unusual-patterned images, such as the example in Fig. 1b. (3) Each low-level feature is usually advantageous only on a specific aspect, e.g. color histogram is good at differentiating texture patterns, while frequency spectrum is good at differentiating energy patterns. It is generally difficult to combine different low-level features into a single algorithm to benefit from them all. Although some integration trials have been made [18], [34], these specially designed algorithms are bulky and inefficient due to the large number of features involved.

On the other hand, the deep neural network (DNN) [35], which has experienced drastic developments in recent years, has shown its powerfulness in extracting high-level features [36], [37], enabling us an excellent machine learning tool to address the aforementioned issues in conventional saliency detection methods. The successes of DNNs stem from their capacity of establishing deep architectures that greatly facilitate the abstraction and learning of complex features among the training data, especially large-scale datasets. There have been initial studies about the application of DNN on the task of saliency detection, such as [2], [38]; these methods, however, are merely using DNNs as binary (i.e. foreground and background) classifiers, with either the original RGB data or hand-crafted features as inputs. This leaves these methods with two drawbacks: (1) Using RGB or low-level feature alone in the saliency classification is non-optimal, as they both have their own advantage and are complementary in representing the images; (2) Using DNNs only as binary classifiers apparently ignores their powerful capacity in dense labeling [37], [39], [40], which is able to directly output a saliency map instead of a single label with the same input data.

In this paper, to utilize the advantages of DNN in complex saliency feature extraction, as well as to address the aforementioned two issues of existing DNN-based methods, we propose a novel DNN-based saliency detection method that conducts both dense and sparse labeling (DSL) with multi-dimensional features. Our method consists of a multi-network framework, which includes three major steps. In the first step, we establish a dense labeling (DL) network, which takes whole images as inputs and directly outputs initial saliency estimations based on macro object contours. In the second step, a sparse labeling (SL) network is established, which outputs another initial saliency estimation based on superpixel-wise low-level image features. The results of DL and SL, together with the original RGB image and a superpixel indication channel, are then integrated as a 6-channeled input structure to the final deep convolutional (DC) network, which is another sparse labeling network that conducts accurate superpixel-wise classification of the final saliency map. Fig. 2 exhibits the flowchart of our proposed DSL method, in which the first two DNNs (DL and SL) are independently trained by the same dataset, while the last DC network takes in the results of DL and SL, and is trained by another dataset due to their serial topology.

Our proposed DSL has the following three key contributions:

(1) The DNN-based dense and sparse labeling are combined for initial saliency estimation in our method, in which DL conducts dense labeling that maximally preserves the global image information and provides accurate location estimation of the salient object, while SL conducts sparse labeling that focuses more on local features of the salient object.

(2) For the two steps that conduct sparse labeling, i.e. SL and DC, both low-level features and RGB features of the image are applied as the network inputs. Such multi-dimensional input features enable the complementary advantage of low-level features and RGB features, by which the image is more accurately abstracted and represented.

(3) In the last DC step, the 6-channeled input structure provides significantly better guidance in generating the final saliency map. On the one hand, the combined initial saliency

estimations from the DL and SL steps provide accurate location guidance of the salient object, effectively excluding any false salient region, as shown in Fig. 1c; on the other hand, the superpixel indication channel precisely represents the current to-be-classified superpixel, which leads to more consistent and accurate saliency labeling (Fig. 1d).

Experiments are conducted against sixteen state-of-the-art saliency detection methods, including ten conventional methods and six learning based methods. The results exhibit dominant advantages of our DSL method in terms of both accuracy and robustness.

The remainder of this paper is organized as follows. Section II briefly reviews related works. Section III describes the details of our proposed DSL method. Section IV presents the experiment results as well as discussion. Finally, Section 0 concludes this paper.

II. Related Works

In this section, we briefly review three categories of related works, namely saliency detection, DNN-based sparse labeling, and DNN-based dense labeling.

A. Saliency Detection

From the perspective of computer vision, the methods of saliency detection are broadly categorized into two groups, namely bottom-up methods and top-down methods.

The bottom-up methods are largely designed for non-task-specific saliency detections [41], in which low-level features are mainly involved as fundamentals for the detections. These features are usually data-driven and hand-crafted. As a pioneer, Itti *et al.* [3] present a center-surround model that integrates color, intensity and orientation at different scales for saliency detection. In the work of Cheng *et al.* [17], pixel-wise color histogram and region-based contrast are utilized in establishing the histogram-based and region-based saliency maps. Achanta *et al.* [21], propose a frequency-tuned method based on color and luminance, in which the saliency value is computed by the color difference with respect to the mean pixel value. Jiang *et al.* [19] establish a 2-ring graph model that calculates saliency values of different image regions by their Markov absorption probabilities. To overcome the negative influence of small-scale high-contrast image patterns, Yan *et al.* [30] propose a multi-layer approach that optimizes saliency detection by a hierarchical tree model. Yang *et al.* [1] exploit the graph-based manifold ranking in extracting foreground queries for the final saliency map, in which the four image boundaries are used as background prior knowledge. In the work of Li *et al.* [42], the image boundaries are refined before being used as background prior knowledge, and a random-walk based ranking model is applied for saliency optimization. And in the work of Qin *et al.* [23], the saliency of different image cells is computed by synchronous update of their dynamic states via the cellular automata model. These bottom-up methods are generally hindered by the aforementioned three limitations of the low-level features.

On the other hand, the top-down saliency detection methods are usually task-driven. These methods break down the saliency detection task into more fundamental components, and task-specific high-level features are frequently involved as prior knowledge. Supervised learning approaches are commonly used in detecting image saliency. In the work of Yang *et al.* [32], joint learning of conditional random field (CRF) is conducted in discriminating visual saliency. Lu *et al.* [43] apply a graph-based diffusion process to learn the optimal seeds of an image to discriminate object and background. Mai *et al.* [44] train a CRF model to aggregate saliency maps from various models, which benefits not only from the individual saliency maps, but also from the interactions among different pixels. And in the work of Tong *et al.* [45], samples from a weak saliency map are exploited as the training set for a series of supply vector machines (SVMs), which are subsequently applied to generate a strong saliency map. Although learning processes are conducted among the top-down saliency detection methods, their high-level features are still mostly extracted via linear approaches, which are insufficient in dealing with the highly-random natural images. On the contrary, in our DSL method, multiple DNN architectures are adopted to extract high-level nonlinear data features, which are experimentally validated to have state-of-the-art performances in various challenging image cases.

B. DNN-Based Sparse Labeling

Deep neural network is a branch of machine learning that has experienced drastic developments in the last decade. First proposed by LeCun *et al.* in 1989 [35], the DNNs, and especially the convolutional neural networks (CNNs), are designed to model high-level nonlinear data features by multiple complex processing layers [46]. DNN is remarkably successful in image classification [5], [47], [48], object detection [37], [39], semantic segmentation [40], [49], [50], face recognition [51], [52], pose estimation [53], and pedestrian behavior estimation [54], [55], etc.

Sparse labeling is the fundamental application of DNN in classification tasks. The idea is to generate a single class label for each input sample [56], such as an image. Many state-of-the-art network models are designed under this scheme, including AlexNet [47], OverFeat [48], Clarifai [57], VGG [58], and GoogLeNet [5], etc. Recently, initial studies have emerged towards the application of DNN in saliency sparse labeling. For instance, Wang *et al.* [38] train two separate DNNs with image patches and object proposals for local and global saliency; Zhao *et al.* [2] establish a multi-context DNN model for superpixel-wise saliency classification; and Li *et al.* [59] propose a multi-scale DNN model for feature extraction, the outputs of which are then aggregated for the final saliency map.

In our proposed DSL method, the SL and DC steps are based on DNN sparse labeling, which generate a single saliency label for each superpixel sample from the input image.

C. DNN-Based Dense Labeling

On the other hand, the dense labeling is a newly arising application of DNN that has drawn much attention. Unlike sparse labeling, dense labeling aims to predict a complete label mask (instead of a single label) based on the input sample, with

The final version of record is available at http://dx.doi.org/10.1109/TCSVT.2016.2646720

either identical or reduced size. Since much more per-sample label information can be generated than sparse labeling, DNN-based dense labeling has greatly facilitated many previously challenging tasks such as object detection and semantic segmentation, in terms of both accuracy and efficiency. In [39], Szegedy *et al.* propose the idea of DNN-based object detection via DNN regression and multi-scale refinements. Girshick *et al.* [37] combine CNNs with bottom-up region proposals to localize and segment objects. Long *et al.* [40] propose the idea of fully convolutional network (FCN), which achieves dramatic improvements in semantic segmentation. And in the work of Chen *et al.* [50], responses from CNNs are combined with fully connected CRF, which overcomes the poor localization property of CNN itself.

In our proposed DSL method, the DL step conducts DNN-based dense labeling that directly outputs an initial saliency estimation of the input image.

III. Proposed Algorithm

As introduced in Section I, our DSL method has three major steps, namely DL, SL and DC, as shown in Fig.2. Considering the topological structure of the three steps, two independent training datasets T_1 and T_2 are used, in which T_1 is used for DL and SL, and T_2 is used for DC.

A. Dense Labeling of Initial Saliency Estimation

Dense labeling is a category of classification in which each pixel in the input image is assigned a label indicating the type of object it most likely belongs to. Saliency detection can be treated as a binary dense labeling case, since the salient (foreground) and background regions can be seen as two separate objects.

We establish our dense labeling baseline model by referring to [40], which has achieved state-of-the-art performance in dense labeling tasks such as semantic segmentation. Our DL network architecture is shown in TABLE I. The main differences between DL and a normal CNN are that DL takes enlarged input images (up to 384*384), and the last few originally fully-connected (fc) layers are converted to 1*1 convolutional layers. As a result, the heatmaps (instead of scalar labels) of foreground and background can be directly generated at layer conv8, both with size 12*12. We then apply the bilinear interpolation to upsample the heatmaps from 12*12 (M_{conv8}) to 224*224 ($M_{deconv32}$), which is the input size of the following DC step. For each to-be-interpolated pixel on $M_{deconv32}$, its upsampled value is calculated by bilinear interpolation of its closest four values on M_{conv8}, as indicated in Fig. 3:

$$M^{l}_{deconv32}(x,y)=\frac{1}{(x_2-x_1)(y_2-y_1)}\begin{pmatrix} M^{l}_{conv8}(x_1,y_1)(x_2-x)(y_2-y) \\ +M^{l}_{conv8}(x_2,y_1)(x-x_1)(y_2-y) \\ +M^{l}_{conv8}(x_1,y_2)(x_2-x)(y-y_1) \\ +M^{l}_{conv8}(x_2,y_2)(x-x_1)(y-y_1) \end{pmatrix}, \qquad (1)$$

where $l \in [0,1]$ stands for the salient (foreground) layer and background layer. Note that all coordinates are normalized to

TABLE I
Architecture of our DL network

Layer	Type	Output Size	Conv (size, channel, pad)	Max Pooling
input	in	384*384*3	N/A	N/A
conv1_1	c+r	384*384*64	3*3,64,1	N/A
conv1_2	c+r+p	192*192*64	3*3,64,1	2*2
conv2_1	c+r	192*192*128	3*3,128,1	N/A
conv2_2	c+r+p	96*96*128	3*3,128,1	2*2
conv3_1	c+r	96*96*256	3*3,256,1	N/A
conv3_2	c+r	96*96*256	3*3,256,1	N/A
conv3_3	c+r+p	48*48*256	3*3,256,1	2*2
conv4_1	c+r	48*48*512	3*3,512,1	N/A
conv4_2	c+r	48*48*512	3*3,512,1	N/A
conv4_3	c+r+p	24*24*512	3*3,512,1	2*2
conv5_1	c+r	24*24*512	3*3,512,1	N/A
conv5_2	c+r	24*24*512	3*3,512,1	N/A
conv5_3	c+r+p	12*12*512	3*3,512,1	2*2
conv6	c+r+d	12*12*4096	7*7,4096,3	N/A
conv7	c+r+d	12*12*4096	1*1,4096,0	N/A
conv8	c	12*12*2	1*1,2,0	N/A
deconv32	us	384*384*2	N/A	N/A
loss	sm+log	1*1	N/A	N/A

Annotations - in: input layer; c: convolutional layer; r: ReLU layer; p: pooling layer; d: dropout layer; us: upsampling layer; sm: softmax layer; log: log loss layer.

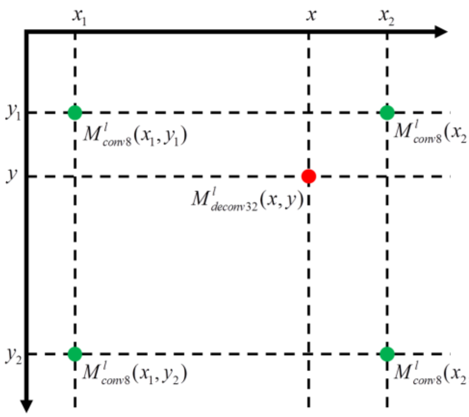

Fig. 3. Bilinear interpolation from the conv8 layer to the deconv32 layer.

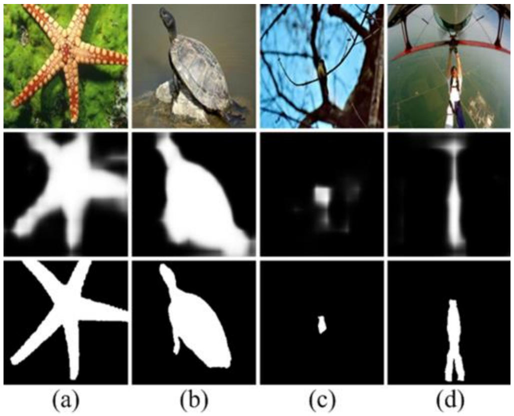

Fig. 4. Example outputs of the DL step. First row: images; second row: outputs of the DL network; third row: ground truth.

[0,1] to facilitate calculation. After that, similar to the softmax regression in normal CNNs, we take each two pixels on $M_{deconv32}$ with the same x and y coordinates (but at different layers) as a pair, and apply the softmax function on them:

$$M_{sm}^{l}(x,y)=\frac{\exp\left(M_{deconv32}^{l}(x,y)\right)}{\sum_{k=0}^{1}\exp\left(M_{deconv32}^{k}(x,y)\right)}. \tag{2}$$

The L2 loss is then computed between the pixel-wise ground truth G and M_{sm}:

$$J_{DL}=\sum_{l=0}^{1}\sum_{x=1}^{X}\sum_{y=1}^{Y}\left(G(x,y)==l\right)\log\left(M_{sm}^{l}(x,y)\right), \tag{3}$$

where "==" means the logical "equal to". Eq. (3) is later used in the back-propagation for training.

As mentioned at the beginning of Section III, the DL network is trained by the training set T_1 . After desired validation results are obtained, it is used to test the training set T_2 , the results of which are then used as part of the 6-channeled inputs in training the DC step, as Fig. 2 shows. Fig. 4 illustrates example outputs of DL. It is observed that DL is capable of producing accurate contours of the salient object, which contains much more boundary information than the bounding box approximation in [39]. In addition, it also has shown high robustness in various challenging scenarios, such as low contrast images (Fig. 4c) and complex images (Fig. 4d).

B. Sparse Labeling of Initial Saliency Estimation

Similar to the DL step which produces initial saliency estimation with macro object contours, the SL step produces initial saliency estimation with low-level image features.

The idea of the SL step is to conduct superpixel-wise sparse labeling of the image based on its corresponding low-level features. Each image is first segmented into superpixels by the SLIC method [60]. We adopt a zoom-out-like feature fusion of each superpixel [49], which consists of 708 local features, 204 neighborhood features, and 4096 global features (5008 features in total for each superpixel).

1) Local Features

The local features are on the smallest scope in our feature extraction, which focus on the current superpixel itself, as the red regions in Fig. 5 indicate. Due to the narrow scope, the local features tend to have large variance among neighboring superpixels. There are 708 local features in total, including 204 color features, 4 location features, and 500 local CNN features.

Color: We first extract the bounding box of the current superpixel, and then calculate its histograms for each of the three channels in both RGB and L*a*b color spaces, with 32 color bins each. In addition, the mean and variance for each of the three channels in the two color spaces are also calculated. This yields 32*3*2 + 2*3*2 = 204 color features.

Location: We compute the min / max x and y coordinates of the current superpixel's bounding box, and conduct normalization to the size of the image. This yields 4 location features in the range of [0, 1].

Local CNN: The last part of local feature is a representation of the current superpixel by a local convolutional network, which is fine-tuned from the LeNet model for hand-written digit recognition [61]. TABLE II shows the architecture of the local CNN, which has four convolutional layers separated by batch normalization [62], max pooling and ReLU layers. It takes the bounding box of the current superpixel in the L*a*b color space as input (resized to 28*28*3), and outputs a binary label that indicates the current superpixel being salient or background. We select the output of conv3, which is the activation value of the last fully connected layer fc4, as the local CNN feature. This yields 500 CNN features.

2) Neighborhood Features

The neighborhood features are on the second scope in our feature extraction, which focuses on the neighboring regions of the current superpixel. The neighboring region is defined as the second order neighboring superpixels of the current superpixel, as the blue regions in Fig. 5 indicates. They are designed to reflect an intermediate level of features of the current superpixel, which are more enriched than the local features, but

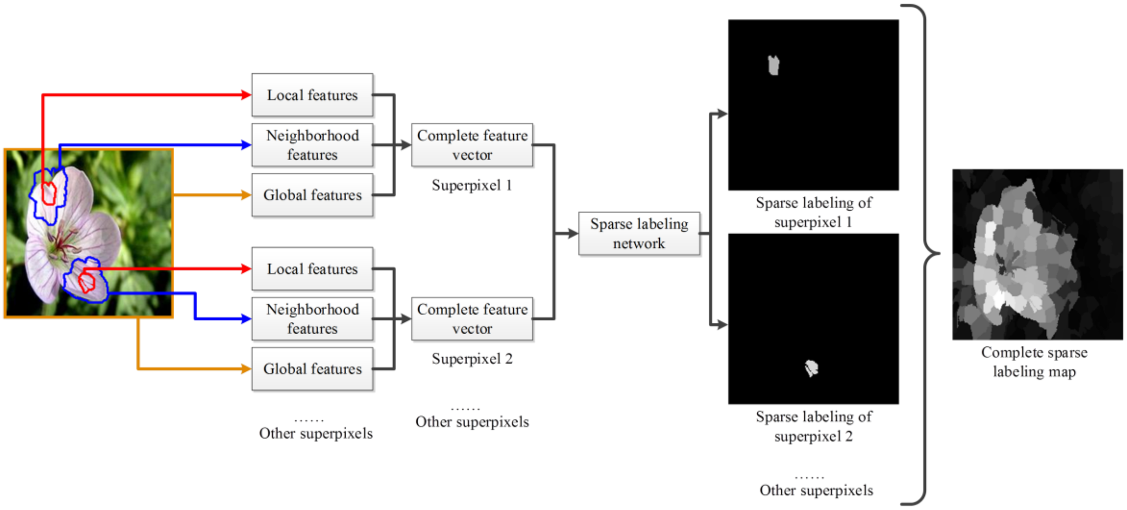

Fig. 5. Flowchart of the SL step. The input image after superpixel segmentation is processed by local, neighborhood and global feature extractions for the complete feature vector. The sparse labeling network then takes in the complete feature vector and conducts image-feature-based initial saliency estimation.

TABLE II
ARCHITECTURE OF OUR LOCAL CNN

Layer	Type	Output Size	Conv (size, channel, pad)	Max Pooling
input	in	28*28*3	N/A	N/A
conv1	c+b+p	12*12*20	5*5,20,0	2*2
conv2	c+b+p	4*4*50	5*5,50,0	2*2
conv3	c+b+r	1*1*500	4*4,500,0	N/A
fc4	fc+r	1*1*2	1*1,2,0	N/A
loss	sm+log	1*1	N/A	N/A

Annotations - in: input layer; c: convolutional layer; b: batch normalization layer; p: pooling layer; r: ReLU layer; fc: fully connected layer; sm: softmax layer; log: log loss layer.

are less macro-scoped than the global features. Due to its definition, the neighborhood features are expected to have lower variance among different superpixels than the local features. We adopt the same set of color features defined in the previous section as the neighborhood features, which yields 204 features.

3) *Global Features*

The global features consist of representations of the whole image, as the yellow region (outer boundary) in Fig. 5 indicates. We use a CNN designed for ImageNet classification to generate the global features. By considering the overall performance, the VGG-16 model [58] is adopted, which is the same model used in the DC step (see Section IV.B for detailed discussion). Images are resized to 224*224 before being fed into the network, and the 1*1*4096 activation value of the last fully connected layer is taken as the global feature. Following [49], we directly use the pre-trained network without fine-tuning.

4) *SL Network Training*

By performing the feature extraction steps above, a 1*5008 feature vector will be generated per superpixel per image. We then establish the SL network with three fully connected layers (see Section IV.B for detailed discussion), which takes the feature vectors as inputs, and output a binary label indicating the saliency of the current superpixel. After training for enough epochs, the SL network is used to generate the low-level feature based initial saliency channel for the next DC step.

C. Sparse Labeling of Final Saliency Map

While the DL and SL steps are designed to provide coarse initial saliency estimations, the DC step is designed to generate the final saliency map with superpixel-wise binary sparse labeling, i.e. obtain the saliency of each individual superpixel in the image via DNN-based classification, and then integrate them together to form the complete final saliency map, as shown in Fig. 2. Considering the overall performance, we adopt the VGG-16 [58] as the baseline model of our DC network (see Section IV.B for detailed discussion). TABLE III shows the architecture of the DC network. The input structure of DC, being one of our key novelties, is 6-channeled data with fixed size as 224*224*6. The first three channels are the RGB data from the image; the fourth and fifth channels are the initial saliency estimations from the DL and SL steps, respectively (both resized to 224*224); and the sixth channel is the superpixel indication channel, which precisely marks the current to-be-classified superpixel, as the “Superpixel indication channel” in Fig. 2 indicates.

TABLE III
ARCHITECTURE OF OUR DC NETWORK

Layer	Type	Output Size	Conv (size, channel, pad)	Max Pooling
input	in	224*224*6	N/A	N/A
conv1_1	c+b+r	224*224*64	3*3,64,1	N/A
conv1_2	c+b+r	112*112*64	3*3,64,1	2*2
conv2_1	c+b+r	112*112*128	3*3,128,1	N/A
conv2_2	c+b+r	56*56*128	3*3,128,1	2*2
conv3_1	c+b+r	56*56*256	3*3,256,1	N/A
conv3_2	c+b+r	56*56*256	3*3,256,1	N/A
conv3_3	c+b+r	28*28*256	3*3,256,1	2*2
conv4_1	c+b+r	28*28*512	3*3,512,1	2*2
conv4_2	c+b+r	28*28*512	3*3,512,1	N/A
conv4_3	c+b+r	14*14*512	3*3,512,1	2*2
conv5_1	c+b+r	14*14*512	3*3,512,1	N/A
conv5_2	c+b+r	14*14*512	3*3,512,1	N/A
conv5_3	c+b+r	7*7*512	3*3,512,1	2*2
fc6	fc+r	1*1*4096	7*7,4096,0	N/A
fc7	fc+r	1*1*4096	1*1,4096,0	N/A
fc8	fc+r	1*1*2	1*1,2,0	N/A
loss	sm+log	1*1	N/A	N/A

Annotations - in: input layer; c: convolutional layer; b: batch normalization layer; p: pooling layer; r: ReLU layer; fc: fully connected layer; sm: softmax layer; log: log loss layer.

To obtain the superpixel indication channel, we first segment the image into superpixels, also by the SLIC method used in Section III.B. The to-be-classified superpixel is then selected and marked on a 224*224 black background, i.e. assigning the pixels within the superpixel as maximum intensity, while all the other pixels remain zero. Note that the superpxiel indication channel is the only channel to differentiate the inputs of different superpixels from the same image. Hence, provided that the number of images and number of superpixels per image are assigned by N_{im} and N_{sp} , respectively, there will be $N_{im} \cdot N_{sp}$ samples in total.

Let Y_i be the activation value of the fc8 layer for the *i*-th superpixel, whose size is changed from the originally 1000 to 2, indicating binary classification (salient or background). A softmax loss layer is applied afterwards to compute the logarithm loss, with N_{sp} as the batch size:

$$J_{DC} = -\frac{1}{N_{sp}} \sum_{i=1}^{N_{sp}} \left[G_i \log P_i + (1 - G_i) \log(1 - P_i) \right] + \lambda_C \sum_j \left(W_j^T W_j \right), \tag{4}$$

where

$$P_i = \frac{\exp\left(Y_i(1)\right)}{\exp\left(Y_i(0)\right) + \exp\left(Y_i(1)\right)} \tag{5}$$

is the softmax probability of i being salient; $G_i \in [0,1]$ is the ground truth label of i ; λ_C is the weight decay parameter; j stands for the layers with trainable weights of the DC network; and W_j is the weight vector of layer j .

We then train DC by the T_2 dataset, as mentioned at the start of Section III, with N_{sp} samples per batch and N_{im} batches in total. As for testing, the probability P_i in (5) is adopted as the saliency value for the superpixel *i*, which is assigned to all the pixels within *i*. And the final saliency map is formed when all

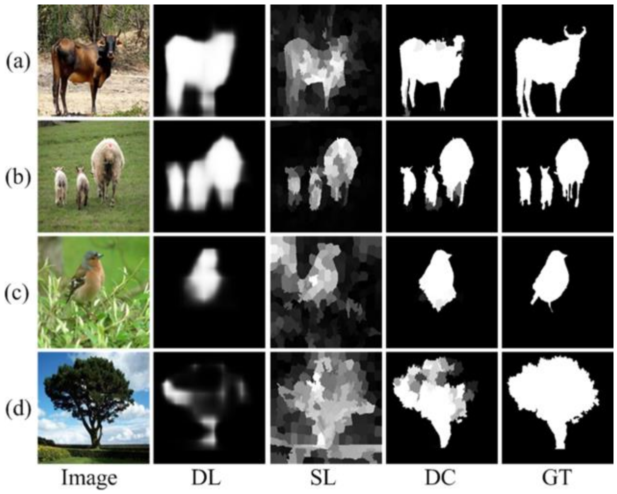

Fig. 6. Example outputs of the DL, SL, and DC steps. Note that DL and SL contributes complementarily to the DC step, which generates the final output of the proposed DSL method.

of the superpixels in the current image have obtained their corresponding saliency values, as indicated in Fig. 2.

The major advantage of DC is attributed to its 6-channeled input structure. Unlike existing DNN-based methods like [2], [38] that only use RGB or other features from the current image itself, DC integrates two coarse guiding channels via dense labeling (DL) and sparse labeling (SL). The two guiding channels provide reliable prior knowledge with learned high-level features from the entire training dataset, and can accurately approximate the salient region as well as exclude false salient proposals. The 6-channeled input structure also contains the superpixel indication channel, which directly and precisely marks the current to-be-classified superpixel, unlike [2] which only vaguely indicates the superpixel by putting it to the image center. The examples in Fig. 6 exhibit the combined strength of the DL, SL and DC steps. Note that DL and SL contribute complementarily to the DC step (i.e. the final output of DSL), especially in cases where one of DL or SL encounters difficulty in estimating the initial saliency accurately, as seen in Fig. 6c and Fig. 6d. The combination of DL and SL thus significantly increases the overall robustness of DSL.

IV. Experiments

A. Experiment Setup

1) Datasets

Since DL and SL are both serially connected to DC (Fig. 2), it is necessary to use two independent training sets for DL / SL and DC respectively, in order to conduct fair trainings.

For the training of DL and SL, we use the DUT-OMRON dataset [1], which contains 5,168 manually selected high quality images and corresponding pixel-wise ground truth. We randomly select 80% of the images for training, and the rest 20% images for validation.

For the training of DC, we use the MSRA10K dataset [17], which contains 10,000 randomly chosen images from the MSRA dataset [13], and their corresponding pixel-wise ground truth. To make the comparison with state-of-the-art methods fair, we follow [2] and randomly choose 80% of the images for training, and the rest 20% images for validation.

For testing, we adopt six well-recognized public datasets, namely ECSSD [30], PASCAL-S [63], SED1 [64], SED2 [64], THUR15K [65], and HKU-IS [59]. The ECSSD dataset contains 1,000 complex images with diversified contexts. The PASCAL-S dataset is a subset of the PASCAL-S VOC segmentation challenge [66], which contains 850 images with highly challenging backgrounds. The SED1 and SED2 are two datasets designed for saliency detection, with 100 images each; the images of SED1 contain one salient object, while the images of SED2 contain two salient objects. The THUR15K dataset contains 15,000 images, among which we only use the 6,233 images with pixel-wise ground truth. For the HKU-IS dataset, we only use the 1,447 images in the test set that have no overlap with any of our comparison methods' training set in our following experiments.

2) Evaluation Metrics

Following a recent saliency detection benchmark [67], we choose the precision-recall (PR) curve, F-measure, and mean absolute error (MAE) as our evaluation metrics.

The precision and recall values are obtained by binarizing the saliency map with integer thresholds between 0 and 255. The precision value equals to the ratio of retrieved salient pixels to all the pixels retrieved, while the recall value equals to the ratio of retrieved salient pixels to all salient pixels in the image. The PR curve is plotted by the precision and recall values at each threshold point.

The F-measure is a weighted average between precision and recall, which is calculated as:

$$F_\beta = \frac{(1+\beta^2)\, precision \cdot recall}{\beta^2\, precision + recall}, \tag{6}$$

where β^2 is set to 0.3 based on most existing methods. As suggested in [68], the average F-measure of a PR curve equals to its maximum single-point F-measure.

The MAE is the mean of the absolute difference between the saliency map S and the pixel-wise ground truth G :

$$MAE = \frac{1}{N}\sum_{i=1}^{N} \left| S(i) - G(i) \right|. \tag{7}$$

Different to precision, recall and F-measure, smaller MAE means higher performance.

3) Implementation

Our method is implemented on MatConvNet [69], which is a MATLAB toolbox of CNN with various extensibilities. The machine used for our experiments is a PC with Intel 6-Core i7-5820K 3.3GHz CPU, 64GB RAM, GeForce GTX TITAN X 12GB GPU, and 64-bit Ubuntu 14.04.3 LTS. Software dependencies include CUDA 7.0 and cuDNN v3. All images are stored on SSD, which accelerates reading speed. The source code of our proposed DSL method is available online: https://github.com/yuanyc06/dsl.

B. Design Option Analyses

1) Parameter of the DL Step

The DL network is trained on the DUT-OMRON dataset for 50 epochs, with 50-point logarithm space between 10^{-3} and 10^{-4} as the learning rate. As described in Section III.A, the images

TABLE IV
PERFORMANCES OF THE PROPOSED DL NETWORK AGAINST TWO STATE-OF-THE-ART DENSE LABELING MODELS

Model	F-Measure	MAE
FCN-8s	0.670	0.149
FCN-16s	0.727	0.137
DL	**0.747**	**0.128**

The F-measures and MAEs are recorded on the validation set at the 50th training epoch. The best results are marked in **red**.

TABLE V
PERFORMANCES OF THE SL NETWORK WITH DIFFERENT LAYER NUMBER (#LAYER) AND PARAMETERS PER LAYER (#PARAM)

Configuration	F-Measure	MAE
#layer=3, #param=1024	0.664	0.182
#layer=3, #param=2048	**0.670**	**0.171**
#layer=3, #param=4096	0.666	0.178
#layer=4, #param=1024	0.661	0.180
#layer=4, #param=2048	0.654	0.186
#layer=4, #param=4096	0.652	0.193

The F-measures and MAEs are recorded on the validation set at the 50th training epoch. The best results are marked in **red**.

TABLE VI
PERFORMANCES OF DSL WITH DIFFERENT SL FEATURE COMBINATIONS

Dataset	Feature of SL	F-Measure	MAE
ECSSD	local	0.783	0.213
	neighborhood	0.778	0.224
	global	0.795	0.181
	local + neighborhood	0.789	0.174
	neighborhood + global	0.801	0.166
	local + global	0.804	0.158
	all	**0.808**	**0.126**
PASCAL-S	local	0.777	0.178
	neighborhood	0.770	0.195
	global	0.782	0.143
	local + neighborhood	0.780	0.162
	neighborhood + global	0.786	0.136
	local + global	0.788	0.131
	all	**0.791**	**0.122**

The best results are marked in **red**.

TABLE VII
PERFORMANCES OF THE DC STEP WITH DIFFERENT BASELINE MODELS ON THE TWO CHALLENGING DATASETS ECSSD AND PASCAL-S

Dataset	Model	F-Measure	MAE
ECSSD	AlexNet	0.802	0.133
	VGG-16	**0.808**	**0.126**
	GoogLeNet	0.807	0.129
PASCAL-S	AlexNet	0.782	0.128
	VGG-16	**0.791**	**0.122**
	GoogLeNet	0.789	0.127

The best results are marked in **red**.

TABLE VIII
PERFORMANCES OF DIFFERENT DESIGN OPTION CONFIGURATIONS ON THE TWO CHALLENGING DATASETS ECSSD AND PASCAL-S

Dataset	Configuration	F-Measure	MAE
ECSSD	Config i: Baseline	0.724	0.187
	Config ii: DC only	0.750	0.171
	Config iii: DL+DC	0.788	0.147
	Config iv: SL+DC	0.772	0.162
	Config v: DL+SL+DC	**0.808**	**0.126**
PASCAL-S	Config i: Baseline	0.681	0.168
	Config ii: DC only	0.729	0.148
	Config iii: DL+DC	0.777	0.140
	Config iv: SL+DC	0.759	0.143
	Config v: DL+SL+DC	**0.791**	**0.122**

The best results are marked in **red**.

are resized to 384*384*3 before put into the network.

To evaluate the network architecture of DL, we compare it against two state-of-the-art dense labeling models extended from [40], namely FCN-8s and FCN-16s. We fine-tune our DL network on each of the three models, and record the performance of the three architectures on the validation set of the 50th epoch. The results are shown in TABLE IV.

It is apparent that the proposed DL architecture has the optimal performance against the other two models, largely due to its less likelihood of over-fitting. Since the original object detection task in [40] was performed on a relatively large dataset (~30K images on the VOC2011 dataset), it was reasonable that the more complex models had higher performances (i.e. FCN-32s < FCN-16s < FCN-8s). On the other hand, in our DL step the training dataset is relatively small (only 5,168 images), thus more complex models are more vulnerable to over-fitting. As a result, it is the less complex model DL (FCN-32s) that performs the best.

2) *Parameter of the SL Step*

There are two networks to train for the SL step, namely the local CNN (Section III.B) and the SL network itself. We randomly select 2,000 images from the DUT-OMRON dataset for the local CNN, and the rest 3,168 images for the SL network. Both networks use 80% of their assigned images for training, and the rest 20% for validation. They are both trained for 50 epochs, with 50-point logarithm space between 10^{-2} and 10^{-4} as the learning rate. We use the SLIC [60] method to generate the superpixels required, with 200 superpixels per image. As described in Section III.B, the input of the local CNN are superpixel patches resized to 28*28*3, while the input of the SL network are 1*5008 feature vectors of the superpixels.

The local CNN is fine-tuned from LeNet [61], and the SL network is trained from scratch (since no baseline model available). To determine the optimal network architecture for SL, we change the network layer number (#layer) and parameter number per layer (#param) 2-dimensionally, and record the validation performances on the 50th training epoch, as shown in TABLE V. The configuration that gives the best performance is #layer=3 + #param=2048, which are adopted in our following experiments.

After determining the network architecture of SL, we further analyze the influence of its three types of features (i.e. local, neighborhood and global features) to the overall performance of our DSL method. The analysis is conducted on the two challenging datasets ECSSD and PASCAL-S, and we use seven different combinations of the features to train the SL network (the feature vector of SL is changed accordingly), and use the corresponding feature combinations in the testing processes. TABLE VI shows the evaluation results, in which using all three types of features contributes to the best performance in terms of both F-measure and MAE on both of the datasets. We thus adopt all three types of features for the SL step.

The final version of record is available at http://dx.doi.org/10.1109/TCSVT.2016.2646720

3) *Parameter of the DC Step*

The DC network is trained on the MSRA10K dataset. We first feedforward MSRA10K through DL and SL to obtain the two initial saliency channels of its images, and then form the 6-channeled inputs for DC. The DC network is trained for 20 epochs, with 20-point logarithm space between 10^{-2} and 10^{-4} as the learning rate. The superpixels are generated by the SLIC method as well, with 200 superpixels per image.

To determine the best baseline model, we fine-tune the DC network on three state-of-the-art image classification models, namely AlexNet [47], VGG-16 [58], and GoogLeNet [5]. We record their performances on the two challenging datasets ECSSD and PASCAL-S in TABLE VII. It is observed that VGG-16 has the best overall performance than the other two models, and previous works have proved its steadiness and robustness in various computer vision tasks [40], [70-72]. We thus adopt VGG-16 as our baseline model for the DC step.

4) *Contribution Comparison*

Next, we examine the contributions of the three steps (i.e. DL, SL and DC) in improving the performance of our method. We take the “pad-and-center” method in [2] as the comparison baseline, and compare five different configurations below:

i. Baseline: the local pad-and-center model in [2]; the network takes padded image as input (224*224*3) (without the superpixel indication channel);

ii. DC only: the input of DC is thus 224*224*4 (with the superpixel indication channel, but without the DL and SL channels);

iii. DL and DC: the input of DC is thus 224*224*5 (with the superpixel indication channel, but without the SL channel);

iv. SL and DC: the input of DC is thus 224*224*5 (with the superpixel indication channel, but without the DL channel);

v. Complete DSL model: the DC network takes the 224*224*6 input with all of the 6 channels.

Similarly to the previous section, we record the performances of the five configurations above on the two challenging datasets ECSSD and PASCAL-S. The results are listed in TABLE VIII. We see that the complete DSL framework (Configuration v: DL+SL+DC) notably outperforms the other four configurations, which indicates that DL, SL and DC all have significant contributions in improving the overall performance of DSL.

C. *Comparison with Conventional Methods*

Next, we compare our proposed DSL method with ten state-of-the-art conventional (non-learning based) saliency detection methods, namely SF [10], GR [73], MC [19], MR [1], DSR [20], HS [30], RBD [25], RR [42], BSCA [23], and BL [45]. All of the ten methods are published after 2012, and the last three methods are recently published in 2015. As mentioned in Section IV.A, the experiments are conducted on the six datasets ECSSD, PASCAL-S, SED1, SED2, THUR15K and HKU-IS. The results are shown in Fig. 7 and TABLE IX.

We first notice that DSL not only achieves the best performance on all of the dataset in terms of both F-measure and MAE, but also exceeds the comparison methods with dominant advantages. We first analyze the two challenging datasets ECSSD and PASCAL-S, where DSL’s PR curves are greatly higher than the comparison methods, and its F-measures and MAEs have shown significantly large gaps against the second best methods. To be more specific, its F-measures are 12.5% and 18.2% higher than the second best (0.808 to 0.718, and 0.791 to 0.669), and its MAEs are 78.6% and 65.6% lower than the second best (0.126 to 0.225, and 0.122 to 0.202). We attribute the greatly improved performance of DSL to its integrated structure of multiple DNNs, in which both dense and sparse labeling show their strength in extracting the high-level features of the image, as well as their combined advantage that further boost the saliency classification accuracy.

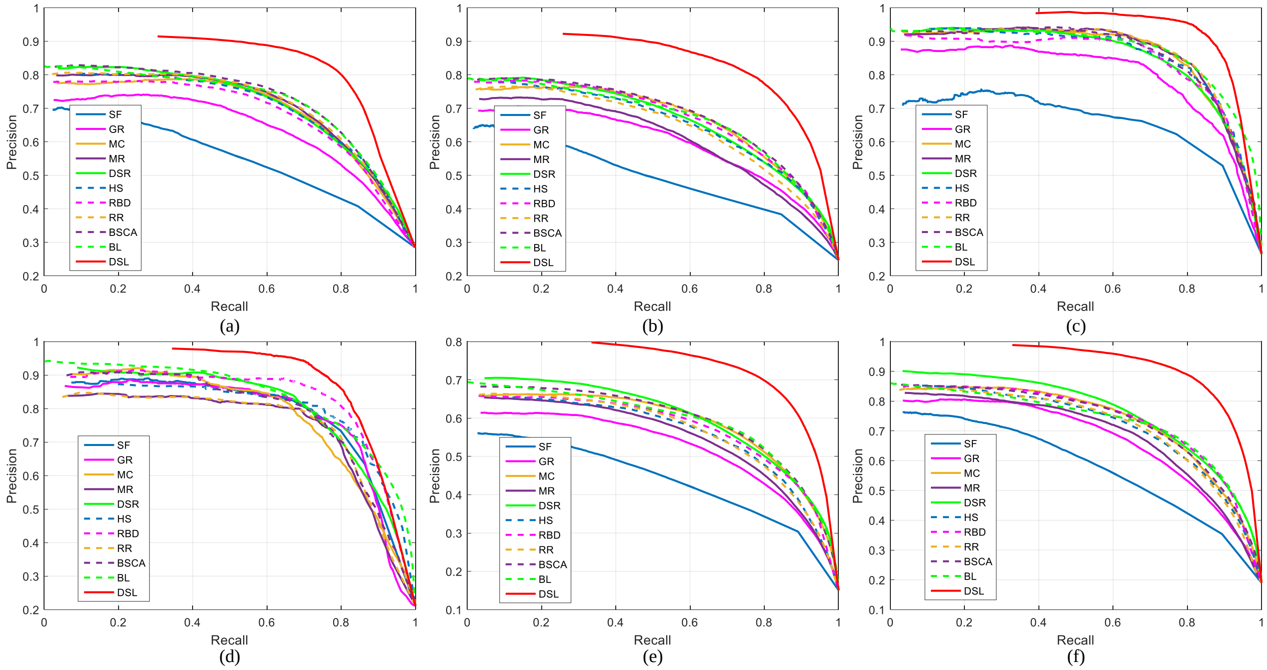

(a) (b) (c) (d) (e) (f)

Fig. 7. PR curves of DSL against ten state-of-the-art conventional saliency detection methods. (a) ECSSD; (b) PASCAL-S; (c) SED1; (d) SED2; (e) THUR15K; (f) HKU-IS.

TABLE IX
QUANTITATIVE EVALUATION RESULTS OF DSL AGAINST TEN STATE-OF-THE-ART CONVENTIONAL SALIENCY DETECTION METHODS

Dataset	Metric	SF	GR	MC	MR	DSR	HS	RBD	RR	BSCA	BL	DSL
ECSSD	F-Measure	0.549	0.642	0.703	0.708	0.699	0.698	0.686	0.710	**0.718**	**0.716**	**0.808**
	MAE	0.268	0.317	0.251	0.236	**0.226**	0.269	**0.225**	0.234	0.233	0.262	**0.126**
PASCAL-S	F-Measure	0.496	0.604	**0.668**	0.612	0.651	0.645	0.659	0.639	**0.669**	0.663	**0.791**
	MAE	0.241	0.301	0.232	0.259	**0.208**	0.264	**0.202**	0.232	0.224	0.249	**0.122**
SED1	F-Measure	0.665	0.791	**0.844**	0.841	0.819	0.825	0.829	**0.843**	0.832	0.840	**0.901**
	MAE	0.234	0.224	0.164	**0.143**	0.160	0.163	0.144	**0.141**	0.155	0.190	**0.099**
SED2	F-Measure	0.783	0.785	0.775	0.771	**0.793**	0.791	**0.826**	0.769	0.780	0.787	**0.858**
	MAE	0.171	0.192	0.180	0.164	**0.140**	0.195	**0.130**	0.161	0.158	0.189	**0.108**
THUR15K	F-Measure	0.469	0.551	**0.610**	0.573	**0.611**	0.585	0.596	0.590	0.609	0.606	**0.730**
	MAE	0.193	0.264	0.199	0.209	**0.139**	0.250	**0.163**	0.185	0.216	0.261	**0.123**
HKU-IS	F-Measure	0.588	0.672	0.723	0.689	**0.735**	0.706	**0.725**	0.711	0.722	0.716	**0.858**
	MAE	0.183	0.266	0.201	0.192	**0.133**	0.253	**0.150**	0.175	0.210	0.257	**0.125**

For each row, the top 3 results are marked in **red**, **blue** and **green**, respectively.

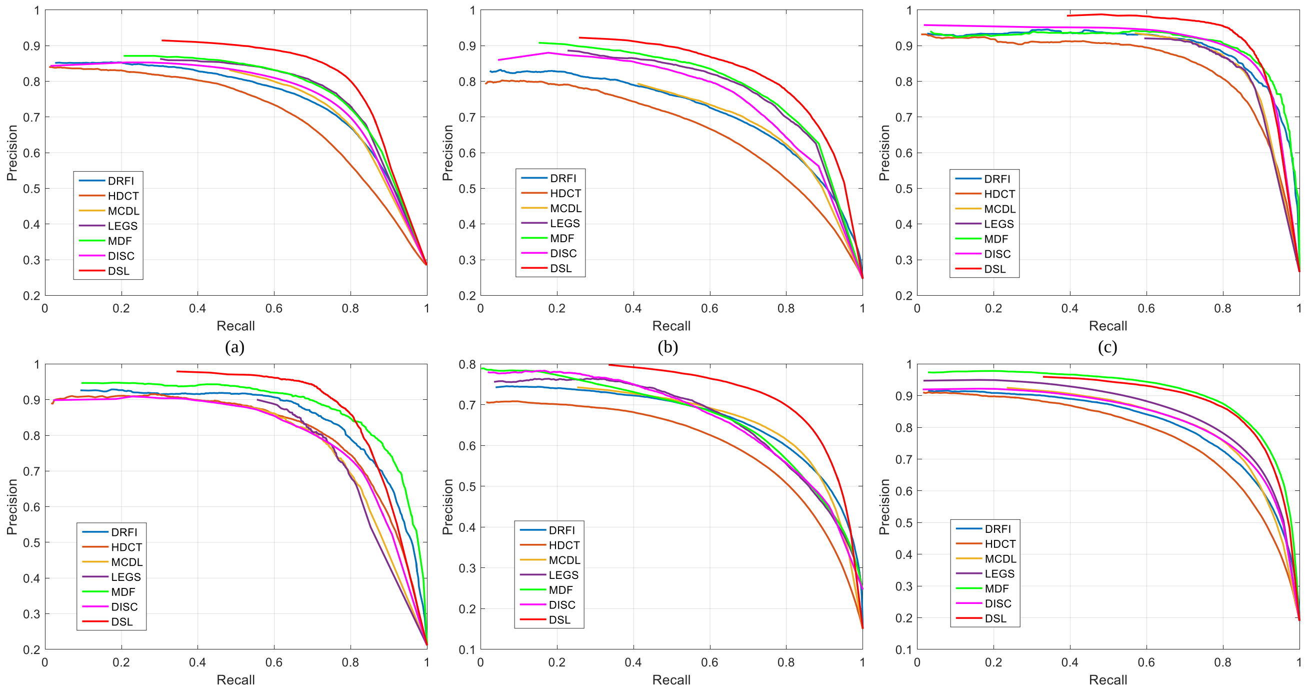

(a) (b) (c) (d) (e) (f)

Fig. 8. PR curves of DSL against six state-of-the-art learning based saliency detection methods. (a) ECSSD; (b) PASCAL-S; (c) SED1; (d) SED2; (e) THUR15K; (f) HKU-IS.

TABLE X
QUANTITATIVE EVALUATION RESULTS OF DSL AGAINST SIX STATE-OF-THE-ART LEARNING BASED SALIENCY DETECTION METHODS

Dataset	Metric	DRFI	HDCT	MCDL	LEGS	MDF	DISC	DSL
ECSSD	F-Measure	0.736	0.698	0.748	**0.776**	**0.772**	0.756	**0.808**
	MAE	0.226	**0.166**	0.175	0.182	**0.174**	0.208	**0.126**
PASCAL-S	F-Measure	0.694	0.652	0.700	**0.762**	**0.768**	0.744	**0.791**
	MAE	0.210	**0.157**	0.160	0.171	**0.144**	0.172	**0.122**
SED1	F-Measure	0.864	0.821	0.858	0.867	**0.881**	**0.876**	**0.901**
	MAE	0.149	0.183	**0.087**	0.185	0.158	**0.118**	**0.099**
SED2	F-Measure	**0.823**	0.792	0.785	0.802	**0.844**	0.780	**0.858**
	MAE	0.140	**0.134**	0.137	**0.104**	0.152	0.153	**0.108**
THUR15K	F-Measure	0.666	0.620	0.673	**0.688**	**0.701**	0.664	**0.730**
	MAE	0.169	0.163	0.192	0.155	**0.140**	**0.084**	**0.123**
HKU-IS	F-Measure	0.775	0.747	0.789	**0.837**	**0.860**	0.788	**0.858**
	MAE	0.161	**0.155**	0.181	**0.146**	0.209	0.180	**0.125**

For each row, the top 3 results are marked in **red**, **blue** and **green**, respectively.

TABLE XI
EFFICIENCY COMPARISON (SECONDS PER IMAGE)

Method	DSR	RBD	LEGS	MDF	DSL
Time (s)	0.525	0.341	1.75	1.48	0.695
Code	MATLAB	MATLAB	MATLAB	MATLAB	MATLAB

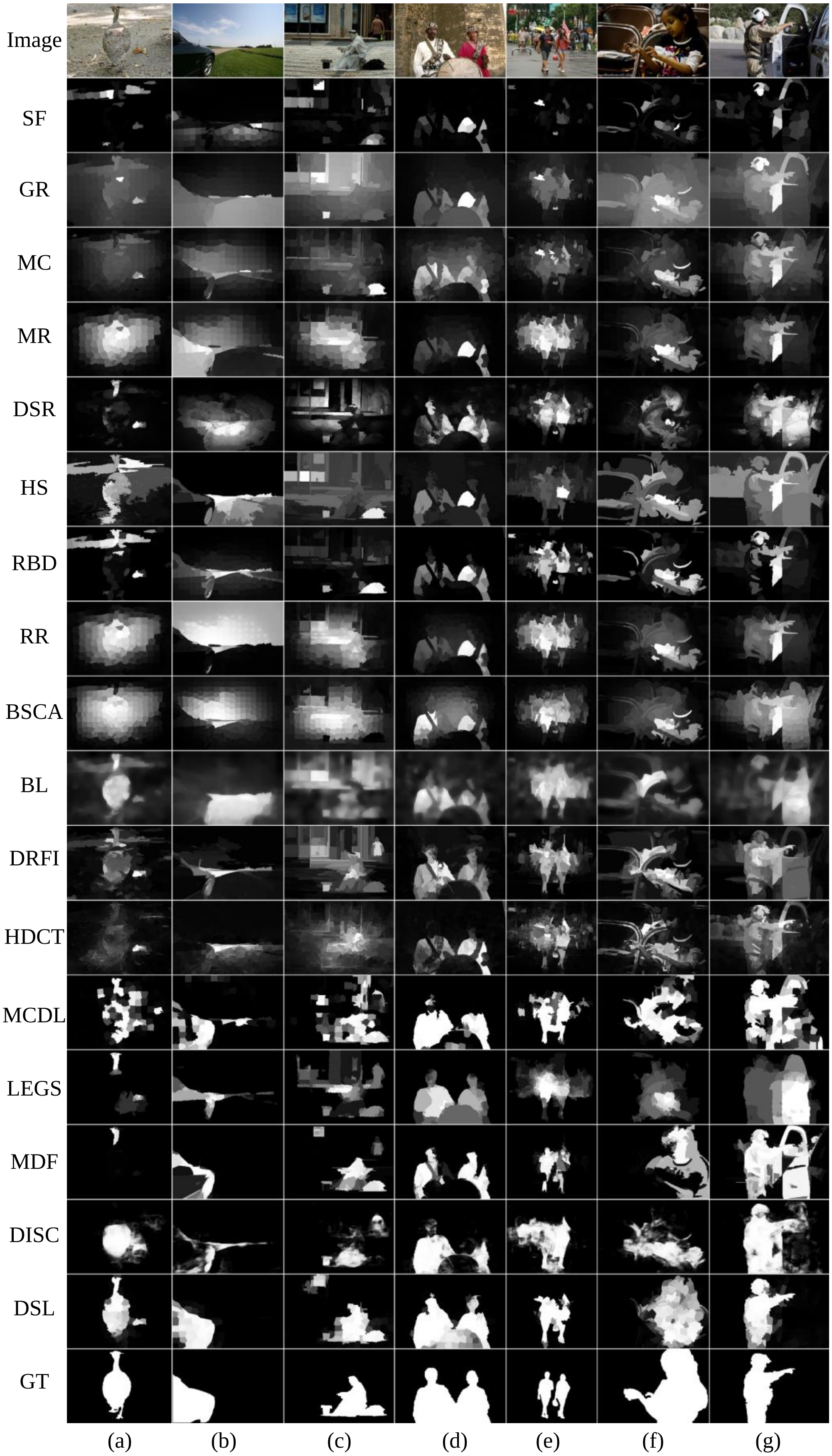

Fig. 9. Example saliency maps of different methods. (a) – (c): images with low contrast objects; (d) – (f): image with complex foreground / background patterns; (g): image with highly interfering background.

DSL behaves similarly on the other four datasets, where it shows dominant advantages on both PR curves and evaluation metrics against all of the comparison methods. What is mentionable is that the advantage of DSL on SED2 is relatively small compared to its advantages on the other datasets. This is mainly due to the single-object training set we used, while all of the images in SED2 contain two salient objects.

D. Comparison with Learning Based Methods

Since DSL is learning based, it is not surprising that it has large performance improvements against the conventional saliency detection methods in Section IV.C. To further evaluate the effectiveness of DSL, we compare it against six state-of-the-art learning based methods, namely DRFI [18], HDCT [74], MCDL [2], LEGS [38], MDF [59] and DISC [70]. All of the six methods are published after 2013, and the last four methods are recently published in 2015. The experiments are conducted on the same six datasets in Section IV.C, and the comparison results are shown in TABLE X.

It is observed that the overall performances of the learning based methods are significantly higher than those of the conventional methods in TABLE IX, due to the high-level features involved in their learning processes. Nevertheless, DSL still maintains significant advantages against the comparison learning based methods. It achieves optimal performance on five out of six F-measures, and three out of six MAEs, and achieves the second place on all of the other evaluations with close distance to the optimal. We note that MDF is the only method that uses the training set of HKU-IS (3,000 images) in its training process, so it is expected to have high performance on the test set of HKU-IS; nevertheless, DSL behaves closely against MDF in F-measure, and even achieves better MAE with significant advantage. We attribute the high performance of DSL to its combination of dense and sparse labeling that exploits both macro object contours and the local low-level image features. DSL's superior performance against the state-of-the-art learning based methods further validates its effectiveness and robustness in various cases.

To demonstrate the greatly improved performance of DSL more straightforwardly, we select typical saliency map examples of both conventional methods and learning based methods, which are assembled together in Fig. 9. We note that DSL exhibits high accuracy and robustness on various challenging scenarios, including images with low contrast objects (Fig. 9a - Fig. 9c), images with complex foreground / background patterns (Fig. 9d - Fig. 9f), and image with highly interfering background (Fig. 9g).

E. Efficiency

To evaluate the efficiency of DSL, we select two comparison methods from both the conventional methods and the learning based methods that have the highest performances among TABLE IX and TABLE X, namely DSR, RBD, LEGS and MDF. We record their average running time per image on the same machine described in Section IV.A.3), and the results are shown in TABLE XI. Since all of the five methods are implemented in MATLAB, the efficiency comparison is fair for coding language. It is observed that besides its premium performances against the comparison methods, DSL also achieves comparable running time to the conventional methods, and notably faster speed than the learning based methods. The three steps of DL, SL and DC take approximately 5%, 60% and 35% of the total running time, respectively.

F. Limitation

As mentioned in Section IV.C, currently DSL's high performance is only guaranteed on single-object images, which is mainly due to the single-object training set we used for the DL, SL and DC networks. This issue, however, is an inherent limitation with all learning based methods that depend on the training data. We can solve this issue by extending our training set with broader categories of images, which will be covered in our future works.

V. Conclusion

In this paper, we propose a novel DNN-based saliency detection method, DSL, which conducts dense and sparse labeling of image saliency with multi-dimensional features. DSL consists of three major steps, namely DL, SL and DC. The DL and SL steps conduct effective initial saliency estimations with both macro object contours and local low-level features, while the final DC network establishes a 6-channeled data structure as input, and conducts accurate final saliency classification. Our DSL method achieves remarkably higher performance against sixteen state-of-the-art saliency detection methods (including ten conventional methods and six learning based methods) on six well-recognized public datasets, in terms of both accuracy and robustness. As future research, we will explore adaptations of our method to other application areas, such as medical image segmentation and video data processing.

References

[1] C. Yang, L. Zhang, H. Lu, X. Ruan, and M.-H. Yang, "Saliency detection via graph-based manifold ranking," in *Proc. IEEE Conf. Comput. Vision Pattern Recognition (CVPR)*, Portland, OR, USA, Jun. 2013, pp. 3166-3173.

[2] R. Zhao, W. Ouyang, H. Li, and X. Wang, "Saliency detection by multi-context deep learning," in *Proc. IEEE Conf. Comput. Vision Pattern Recognition (CVPR)*, Boston, MA, USA, Jun. 2015, pp. 1265-1274.

[3] L. Itti, C. Koch, and E. Niebur, "A model of saliency-based visual attention for rapid scene analysis," *IEEE Trans. Pattern Anal. Mach. Intell.*, vol. 20, no. 11, pp. 1254-1259, Nov. 1998.

[4] C. Rother, V. Kolmogorov, and A. Blake, "Grabcut: Interactive foreground extraction using iterated graph cuts," *ACM Trans. Graph.*, vol. 23, no. 3, pp. 309-314, Sep. 2004.

[5] C. Szegedy, W. Liu, Y. Jia, P. Sermanet, S. Reed, D. Anguelov, *et al.*, "Going deeper with convolutions," *arXiv preprint arXiv:1409.4842*, 2014.

[6] U. Rutishauser, D. Walther, C. Koch, and P. Perona, "Is bottom-up attention useful for object recognition?," in *Proc. IEEE Conf. Comput. Vision Pattern Recognition (CVPR)*, Washington, D.C., USA, Jun. 2004, pp. II-37-II-44 Vol. 2.

[7] V. Mahadevan and N. Vasconcelos, "Saliency-based discriminant tracking," in *Proc. IEEE Conf. Comput. Vision Pattern Recognition (CVPR)*, Miami, FL, USA, Jun. 2009, pp. 1007-1013.

[8] J. Wang, L. Quan, J. Sun, X. Tang, and H.-Y. Shum, "Picture collage," in *Proc. IEEE Conf. Comput. Vision Pattern Recognition (CVPR)*, New York City, NY, USA, Jun. 2006, pp. 347-354.

[9] T. Wang, T. Mei, X.-S. Hua, X.-L. Liu, and H.-Q. Zhou, "Video collage: A novel presentation of video sequence," in *Proc. IEEE Int. Conf. Multimedia Expo (ICME)*, Beijing, China, Jul. 2007, pp. 1479-1482.

[10] F. Perazzi, P. Krahenbuhl, Y. Pritch, and A. Hornung, "Saliency filters: Contrast based filtering for salient region detection," in *Proc. IEEE Conf. Comput. Vision Pattern Recognition (CVPR)*, Providence, RI, USA, Jun. 2012, pp. 733-740.

[11] P. Wang, D. Zhang, J. Wang, Z. Wu, X.-S. Hua, and S. Li, "Color filter for image search," in *Proc. ACM Int. Conf. Multimedia (ACMMM)*, Nara, Japan, Oct. 2012, pp. 1327-1328.

[12] T. Judd, K. Ehinger, F. Durand, and A. Torralba, "Learning to predict where humans look," in *Proc. IEEE Int. Conf. Comput. Vision (ICCV)*, Kyoto, Japan, Sep. 2009, pp. 2106-2113.

[13] T. Liu, Z. Yuan, J. Sun, J. Wang, N. Zheng, X. Tang, *et al.*, "Learning to detect a salient object," *IEEE Trans. Pattern Anal. Mach. Intell.*, vol. 33, no. 2, pp. 353-367, 2011.

[14] C. Shen and Q. Zhao, "Learning to predict eye fixations for semantic contents using multi-layer sparse network," *Neurocomput.*, vol. 138, pp. 61-68, 2014.

[15] P. F. Felzenszwalb and D. P. Huttenlocher, "Efficient graph-based image segmentation," *Int. J. Comput. Vis.*, vol. 59, no. 2, pp. 167-181, 2004.

[16] R. Fergus, P. Perona, and A. Zisserman, "Object class recognition by unsupervised scale-invariant learning," in *Proc. IEEE Conf. Comput. Vision Pattern Recognition (CVPR)*, Madison, WI, USA, Jun. 2003, pp. II-264-II-271 vol. 2.

[17] M.-M. Cheng, G.-X. Zhang, N. J. Mitra, X. Huang, and S.-M. Hu, "Global contrast based salient region detection," in *Proc. IEEE Conf. Comput. Vision Pattern Recognition (CVPR)*, Colorado Springs, CO, USA, Jun. 2011, pp. 409-416.

[18] H. Jiang, J. Wang, Z. Yuan, Y. Wu, N. Zheng, and S. Li, "Salient object detection: A discriminative regional feature integration approach," in *Proc. IEEE Conf. Comput. Vision Pattern Recognition (CVPR)*, Portland, OR, USA, Jun. 2013, pp. 2083-2090.

[19] B. Jiang, L. Zhang, H. Lu, C. Yang, and M.-H. Yang, "Saliency detection via absorbing markov chain," in *Proc. IEEE Int. Conf. Comput. Vision (ICCV)*, Sydney, NSW, Australia, Dec. 2013, pp. 1665-1672.

[20] X. Li, H. Lu, L. Zhang, X. Ruan, and M.-H. Yang, "Saliency detection via dense and sparse reconstruction," in *Proc. IEEE Int. Conf. Comput. Vision (ICCV)*, Sydney, NSW, Australia, Dec. 2013, pp. 2976-2983.

[21] R. Achanta, S. Hemami, F. Estrada, and S. Susstrunk, "Frequency-tuned salient region detection," in *Proc. IEEE Conf. Comput. Vision Pattern Recognition (CVPR)*, Miami, FL, USA, Jun. 2009, pp. 1597-1604.

[22] X. Hou and L. Zhang, "Saliency detection: A spectral residual approach," in *Proc. IEEE Conf. Comput. Vision Pattern Recognition (CVPR)*, Minneapolis, MN, USA, Jun. 2007, pp. 1-8.

[23] Y. Qin, H. Lu, Y. Xu, and H. Wang, "Saliency detection via cellular automata," in *Proc. IEEE Conf. Comput. Vision Pattern Recognition (CVPR)*, Boston, MA, USA, Jun. 2015, pp. 110-119.

[24] Y. Wei, F. Wen, W. Zhu, and J. Sun, "Geodesic saliency using background priors," in *Comput. Vision–ECCV*, ed: Springer, 2012, pp. 29-42.

[25] W. Zhu, S. Liang, Y. Wei, and J. Sun, "Saliency Optimization from Robust Background Detection," in *Proc. IEEE Conf. Comput. Vision Pattern Recognition (CVPR)*, Columbus, OH, USA, Jun. 2014, pp. 2814-2821.

[26] K.-Y. Chang, T.-L. Liu, H.-T. Chen, and S.-H. Lai, "Fusing generic objectness and visual saliency for salient object detection," in *Proc. IEEE Conf. Comput. Vision Pattern Recognition (CVPR)*, Colorado Springs, CO, USA, Jun. 2011, pp. 914-921.

[27] S. Goferman, L. Zelnik-Manor, and A. Tal, "Context-aware saliency detection," *IEEE Trans. Pattern Anal. Mach. Intell.*, vol. 34, no. 10, pp. 1915-1926, Oct. 2012.

[28] J. Harel, C. Koch, and P. Perona, "Graph-based visual saliency," in *Adv. Neural Inform. Process. Sys.*, Dec. 2006, pp. 545-552.

[29] E. Rahtu, J. Kannala, M. Salo, and J. Heikkilä, "Segmenting salient objects from images and videos," in *Comput. Vision–ECCV*, ed: Springer, 2010, pp. 366-379.

[30] Q. Yan, L. Xu, J. Shi, and J. Jia, "Hierarchical saliency detection," in *Proc. IEEE Conf. Comput. Vision Pattern Recognition (CVPR)*, Portland, OR, USA, Jun. 2013, pp. 1155-1162.

[31] L. Zhang, M. H. Tong, T. K. Marks, H. Shan, and G. W. Cottrell, "SUN: A Bayesian framework for saliency using natural statistics," *J. Vis.*, vol. 8, no. 7, p. 32, 2008.

[32] J. Yang and M.-H. Yang, "Top-down visual saliency via joint crf and dictionary learning," in *Proc. IEEE Conf. Comput. Vision Pattern Recognition (CVPR)*, Providence, RI, USA, Jun. 2012, pp. 2296-2303.

[33] D. A. Klein and S. Frintrop, "Center-surround divergence of feature statistics for salient object detection," in *Proc. IEEE Int. Conf. Comput. Vision (ICCV)*, Barcelona, Spain, Nov. 2011, pp. 2214-2219.

[34] K. Fu, C. Gong, J. Yang, Y. Zhou, and I. Yu-Hua Gu, "Superpixel based color contrast and color distribution driven salient object detection," *Signal Process. Image Commun.*, vol. 28, no. 10, pp. 1448-1463, Jul. 2013.

[35] Y. LeCun, B. Boser, J. S. Denker, D. Henderson, R. E. Howard, W. Hubbard, *et al.*, "Backpropagation applied to handwritten zip code recognition," *Neural Computation*, vol. 1, no. 4, pp. 541-551, 1989.

[36] G. E. Hinton and R. R. Salakhutdinov, "Reducing the dimensionality of data with neural networks," *Sci.*, vol. 313, no. 5786, pp. 504-507, 2006.

[37] R. Girshick, J. Donahue, T. Darrell, and J. Malik, "Rich feature hierarchies for accurate object detection and semantic segmentation," in *Proc. IEEE Conf. Comput. Vision Pattern Recognition (CVPR)*, Columbus, OH, USA, Jun. 2014, pp. 580-587.

[38] L. Wang, H. Lu, X. Ruan, and M.-H. Yang, "Deep networks for saliency detection via local estimation and global search," in *Proc. IEEE Conf. Comput. Vision Pattern Recognition (CVPR)*, Boston, MA, USA, Jun. 2015, pp. 3183-3192.

[39] C. Szegedy, A. Toshev, and D. Erhan, "Deep neural networks for object detection," in *Adv. Neural Inform. Process. Sys.*2013, pp. 2553-2561.

[40] J. Long, E. Shelhamer, and T. Darrell, "Fully convolutional networks for semantic segmentation," *arXiv preprint arXiv:1411.4038*, 2014.

[41] J. Sun, H. Lu, and X. Liu, "Saliency Region Detection Based on Markov Absorption Probabilities," *IEEE Trans. Image Process.*, vol. 24, no. 5, pp. 1639-1649, 2015.

[42] C. Li, Y. Yuan, W. Cai, Y. Xia, and D. D. Feng, "Robust saliency detection via regularized random walks ranking," in *Proc. IEEE Conf. Comput. Vision Pattern Recognition (CVPR)*, Boston, MA, USA, Jun. 2015, pp. 2710-2717.

[43] S. Lu, V. Mahadevan, and N. Vasconcelos, "Learning Optimal Seeds for Diffusion-based Salient Object Detection," in *Proc. IEEE Conf. Comput. Vision Pattern Recognition (CVPR)*, Portland, OR, USA, Jun. 2013, pp. 2790-2797.

[44] L. Mai, Y. Niu, and F. Liu, "Saliency aggregation: A data-driven approach," in *Proc. IEEE Conf. Comput. Vision Pattern Recognition (CVPR)*, Portland, OR, USA, Jun. 2013, pp. 1131-1138.

[45] N. Tong, H. Lu, X. Ruan, and M.-H. Yang, "Salient object detection via bootstrap learning," in *Proc. IEEE Conf. Comput. Vision Pattern Recognition (CVPR)*, Boston, MA, USA, Jun. 2015, pp. 1884-1892.

[46] L. Deng and D. Yu, "Deep learning: methods and applications," *Found. Trends Signal Process.*, vol. 7, no. 3–4, pp. 197-387, 2014.

[47] A. Krizhevsky, I. Sutskever, and G. E. Hinton, "Imagenet classification with deep convolutional neural networks," in *Adv. Neural Inform. Process. Sys.*2012, pp. 1097-1105.

[48] P. Sermanet, D. Eigen, X. Zhang, M. Mathieu, R. Fergus, and Y. LeCun, "Overfeat: Integrated recognition, localization and detection using convolutional networks," *arXiv preprint arXiv:1312.6229*, 2013.

[49] M. Mostajabi, P. Yadollahpour, and G. Shakhnarovich, "Feedforward semantic segmentation with zoom-out features," *arXiv preprint arXiv:1412.0774*, 2014.

[50] L.-C. Chen, G. Papandreou, I. Kokkinos, K. Murphy, and A. L. Yuille, "Semantic image segmentation with deep convolutional nets and fully connected crfs," *arXiv preprint arXiv:1412.7062*, 2014.

[51] Y. Sun, X. Wang, and X. Tang, "Deep convolutional network cascade for facial point detection," in *Proc. IEEE Conf. Comput. Vision Pattern Recognition (CVPR)*, Portland, OR, USA, Jun. 2013, pp. 3476-3483.

[52] Y. Sun, X. Wang, and X. Tang, "Deep learning face representation from predicting 10,000 classes," in *Proc. IEEE Conf. Comput. Vision Pattern Recognition (CVPR)*, Columbus, OH, USA, Jun. 2014, pp. 1891-1898.

[53] A. Toshev and C. Szegedy, "Deeppose: Human pose estimation via deep neural networks," in *Proc. IEEE Conf. Comput. Vision Pattern Recognition (CVPR)*, Columbus, OH, USA, Jun. 2014, pp. 1653-1660.

[54] P. Sermanet, K. Kavukcuoglu, S. Chintala, and Y. LeCun, "Pedestrian detection with unsupervised multi-stage feature learning," in *Proc. IEEE Conf. Comput. Vision Pattern Recognition (CVPR)*, Portland, OR, USA, Jun. 2013, pp. 3626-3633.

[55] X. Zeng, W. Ouyang, and X. Wang, "Multi-stage contextual deep learning for pedestrian detection," in *Proc. IEEE Int. Conf. Comput. Vision (ICCV)*, Sydney, NSW, Australia, Dec. 2013, pp. 121-128.

[56] P. O. Pinheiro and R. Collobert, "From Image-level to Pixel-level Labeling with Convolutional Networks," in *Proc. IEEE Conf. Comput. Vision Pattern Recognition (CVPR)*, Boston, MA, USA, Jun. 2015, pp. 1713-1721.

[57] M. D. Zeiler and R. Fergus, "Visualizing and understanding convolutional networks," in *Comput. Vision–ECCV*, ed: Springer, 2014, pp. 818-833.

[58] K. Simonyan and A. Zisserman, "Very deep convolutional networks for large-scale image recognition," *arXiv preprint arXiv:1409.1556*, 2014.

[59] G. Li and Y. Yu, "Visual Saliency Based on Multiscale Deep Features," *arXiv preprint arXiv:1503.08663*, 2015.

[60] R. Achanta, A. Shaji, K. Smith, A. Lucchi, P. Fua, and S. Susstrunk, "SLIC superpixels compared to state-of-the-art superpixel methods," *IEEE Trans. Pattern Anal. Mach. Intell.*, vol. 34, no. 11, pp. 2274-2282, Nov. 2012.

[61] Y. LeCun, L. Bottou, Y. Bengio, and P. Haffner, "Gradient-based learning applied to document recognition," *Proc. IEEE*, vol. 86, no. 11, pp. 2278-2324, 1998.

[62] S. Ioffe and C. Szegedy, "Batch normalization: Accelerating deep network training by reducing internal covariate shift," *arXiv preprint arXiv:1502.03167*, 2015.

[63] Y. Li, X. Hou, C. Koch, J. Rehg, and A. Yuille, "The secrets of salient object segmentation," in *Proc. IEEE Conf. Comput. Vision Pattern Recognition (CVPR)*, Columbus, OH, USA, Jun. 2014, pp. 4321-4328.

[64] S. Alpert, M. Galun, R. Basri, and A. Brandt, "Image segmentation by probabilistic bottom-up aggregation and cue integration," in *Proc. IEEE Conf. Comput. Vision Pattern Recognition (CVPR)*, Minneapolis, MN, USA, Jun. 2007, pp. 1-8.

[65] M.-M. Cheng, N. J. Mitra, X. Huang, and S.-M. Hu, "Salientshape: Group saliency in image collections," *Visual Comput.*, vol. 30, no. 4, pp. 443-453, 2014.

[66] M. Everingham, L. Van Gool, C. K. Williams, J. Winn, and A. Zisserman, "The pascal visual object classes (voc) challenge," *Int. J. Comput. Vis.*, vol. 88, no. 2, pp. 303-338, Sep. 2010.

[67] A. Borji, D. N. Sihite, and L. Itti, "Salient object detection: A benchmark," in *Comput. Vision–ECCV*, ed: Springer, 2012, pp. 414-429.

[68] D. R. Martin, C. C. Fowlkes, and J. Malik, "Learning to detect natural image boundaries using local brightness, color, and texture cues," *IEEE Trans. Pattern Anal. Mach. Intell.*, vol. 26, no. 5, pp. 530-549, May. 2004.

[69] A. Vedaldi and K. Lenc, "MatConvNet-convolutional neural networks for MATLAB," *arXiv preprint arXiv:1412.4564*, 2014.

[70] T. Chen, L. Lin, L. Liu, X. Luo, and X. Li, "DISC: Deep Image Saliency Computing via Progressive Representation Learning," *arXiv preprint arXiv:1511.04192*, 2015.

[71] R. Girshick, "Fast r-cnn," in *Proc. IEEE Int. Conf. Comput. Vision (ICCV)*, Santiago, Chile, Dec. 2015, pp. 1440-1448.

[72] J. Dai, Y. Li, K. He, and J. Sun, "R-FCN: Object Detection via Region-based Fully Convolutional Networks," *arXiv preprint arXiv:1605.06409*, 2016.

[73] C. Yang, L. Zhang, and H. Lu, "Graph-regularized saliency detection with convex-hull-based center prior," *IEEE Signal Process. Lett.*, vol. 20, no. 7, pp. 637-640, 2013.

[74] J. Kim, D. Han, Y.-W. Tai, and J. Kim, "Salient region detection via high-dimensional color transform," in *Proc. IEEE Conf. Comput. Vision Pattern Recognition (CVPR)*, Columbus, OH, USA, Jun. 2014, pp. 883-890.

Yuchen Yuan received the B. E. degree in biomedical engineering from Tsinghua University, Beijing, China, in 2010, and the M. S. degree in biomedical engineering from Washington University in St. Louis, St. Louis, MO, USA, in 2012. He then worked as a senior system research engineer at Mindray Co., Ltd, Shenzhen, China, from 2012 to 2014.

He is currently a Ph. D. candidate at the School of Information Technologies, the University of Sydney. His research interests include deep learning, saliency detection, image segmentation and bioinformatics.

Changyang Li received the Ph.D. degree from the University of Sydney, Sydney, Australia, in 2012.

He is currently a Research Associate with the School of Information Technologies, the University of Sydney. His current research interests include image segmentation, pattern recognition, processing for biomedical images, and multimodality data registration.

Jinman Kim received the B. S. (honours) and Ph. D. degrees in computer science from the University of Sydney, Sydney, Australia, in 2001 and 2006, respectively. Since his Ph. D., he has been a research associate at the leading teaching hospital, the Royal Prince Alfred. From 2008 to 2012, he was an ARC postdoc research fellow, one year leave (2009-2010) to join the MIRALab research group, Geneva, Switzerland, as a Marie Curie senior research fellow. Since 2013, he has been with the School of IT, the University of Sydney, where he was a senior lecturer, and became an associate professor in 2016.

His research interests include medical image analysis and visualization, computer aided diagnosis, and Telehealth technologies.

Weidong Cai received the Ph. D. degree in Computer Science from the Basser Department of Computer Science, The University of Sydney, Sydney, Australia, in 2001.

He is currently an Associate Professor in the School of Information Technologies, Director of the Multimedia Laboratory in The University of Sydney. He has been a Lead Investigator / Visiting Professor on medical image analysis and medical computer vision at Surgical Planning Laboratory (SPL), Harvard Medical School during his 2014 SSP. His research interests include multimedia computing, medical image analysis, image / video processing and retrieval, computer vision & pattern recognition, big data mining, bioimaging informatics, and computational neuroscience.

Dagan Feng received the M. E. degree in Electrical Engineering & Computer Science (EECS) from Shanghai Jiao Tong University, Shanghai, China, in 1982, and the M. S. in Biocybernetics and Ph. D. in Computer Science from the University of California, Los Angeles, CA, USA, in 1985 and 1988 respectively, where he received the Crump Prize for Excellence in Medical Engineering.

He is currently a Professor in the School of Information Technologies, Director of Biomedical & Multimedia Information Technology (BMIT) Research Group and Director of the Institute of Biomedical Engineering and Technology at the University of Sydney. He has published over 800 scholarly research papers, pioneered several new research directions, and made a number of landmark contributions in his field. Prof. Feng's research in the areas of biomedical and multimedia information technology seeks to address the major challenges in “big data science” and provide innovative solutions for stochastic data acquisition, compression, storage, management, modeling, fusion, visualization and communication. Prof. Feng is Fellow of ACS, HKIE, IET, IEEE and Australian Academy of Technological Sciences and Engineering.